



**HAL**  
open science

# Understanding fast macroscale fracture from microcrack post mortem patterns

Claudia Guerra, Julien Scheibert, Daniel Bonamy, Davy Dalmas

► **To cite this version:**

Claudia Guerra, Julien Scheibert, Daniel Bonamy, Davy Dalmas. Understanding fast macroscale fracture from microcrack post mortem patterns. 2011. hal-00640035v1

**HAL Id: hal-00640035**

**<https://hal.science/hal-00640035v1>**

Preprint submitted on 10 Nov 2011 (v1), last revised 28 Mar 2012 (v2)

**HAL** is a multi-disciplinary open access archive for the deposit and dissemination of scientific research documents, whether they are published or not. The documents may come from teaching and research institutions in France or abroad, or from public or private research centers.

L'archive ouverte pluridisciplinaire **HAL**, est destinée au dépôt et à la diffusion de documents scientifiques de niveau recherche, publiés ou non, émanant des établissements d'enseignement et de recherche français ou étrangers, des laboratoires publics ou privés.

# Understanding fast macroscale fracture from microcrack *post mortem* patterns

C. Guerra,<sup>1,2</sup> J. Scheibert,<sup>1,3,4,5</sup> D. Bonamy,<sup>1</sup> and D. Dalmas<sup>3</sup>

<sup>1</sup>CEA, IRAMIS, SPCSI, Group Complex Systems & Fracture, F-91191 Gif sur Yvette, France

<sup>2</sup>Facultad de Ingeniería Mecánica y Eléctrica, Universidad Autónoma de Nuevo León, Avenida Universidad, S/N, Ciudad Universitaria, C.P. 66450, San Nicolás de los Garza, NL, Mexico

<sup>3</sup>Unité Mixte CNRS/Saint-Gobain, Surface du Verre et Interfaces, 39 Quai Lucien Lefranc, 93303 Aubervilliers cedex, France

<sup>4</sup>Physics of Geological Processes, University of Oslo, P.O. Box 1048 Blindern, 0316 Oslo, Norway

<sup>5</sup>Laboratoire de Tribologie et Dynamique des Systèmes, CNRS, Ecole Centrale de Lyon, 36 Avenue Guy de Collongue, 69134 Ecully, France

Dynamic crack propagation drives catastrophic solid failures. In many amorphous brittle materials, sufficiently fast crack growth involves small-scale, high-frequency microcracking damage localized near the crack tip. The ultra-fast dynamics of microcrack nucleation, growth and coalescence is inaccessible experimentally and fast crack propagation was therefore studied only as a macroscale average. Here, we overcome this limitation in polymethylmethacrylate, the archetype of brittle amorphous materials: We reconstruct the complete spatio-temporal microcracking dynamics, with micrometer / nanosecond resolution, through *post mortem* analysis of the fracture surfaces. We find that all individual microcracks propagate at the same low, load-independent, velocity. Collectively, the main effect of microcracks is not to slow down fracture by increasing the energy required for crack propagation, as commonly believed, but on the contrary to boost the macroscale velocity through an acceleration factor selected on geometric grounds. Our results emphasize the key role of damage-related internal variables in the selection of macroscale fracture dynamics.

The fracture of brittle amorphous materials is usually described using the linear elastic fracture mechanics (LEFM) framework [1–4], which considers the straight propagation of a single smooth crack. All dissipative processes (*e.g.* plastic deformation or bond breaking) are assumed to be localized in a small zone around the crack tip (fracture process zone, FPZ). Crack velocity,  $v$ , is then predicted from the balance between the flux of mechanical energy released from the surrounding elastic material into the FPZ [5], and the dissipation rate within this zone. The former is computable within continuum theory and connects to the stress intensity factor,  $K$ , which describes the macroscopic forcing applying on the crack tip and depends on the external loading and specimen geometry only. The dissipation rate is quantified by the fracture energy,  $\Gamma$ , required to expose a new unit area of cracked surfaces, to be measured experimentally. The resulting equation of motion reads [1]  $\Gamma \approx (1 - v/c_R)K^2/E$  where  $E$  and  $c_R$  denote the material's Young's modulus and Rayleigh wave speed, respectively.

Polymethylmethacrylate (PMMA) is often considered as the archetype of nominally brittle materials and, therefore, has been one of the most widely used materials against which theories have been confronted from the early stages of fracture mechanics. Yet, in PMMA, single smooth cracks are actually observed for slow propagation only. Fast enough cracks ( $v > v_a \sim 0.2 c_R$  [6]) propagate through the nucleation, growth and coalescence, in the fracture plane, of individual microcracks [6–9]. Cracks faster than  $v_b \sim 0.4 c_R$  also involve aborted out-of-plane secondary cracks known as microbranches [2, 10, 11], which prevent LEFM from being applicable

[11]. LEFM has been shown to agree with experiments as long as no microbranch is involved [6, 11–13], *i.e.* even in the presence of microcracks, provided a suitable velocity dependence of the fracture energy,  $\Gamma(v)$ , is prescribed [6, 11].

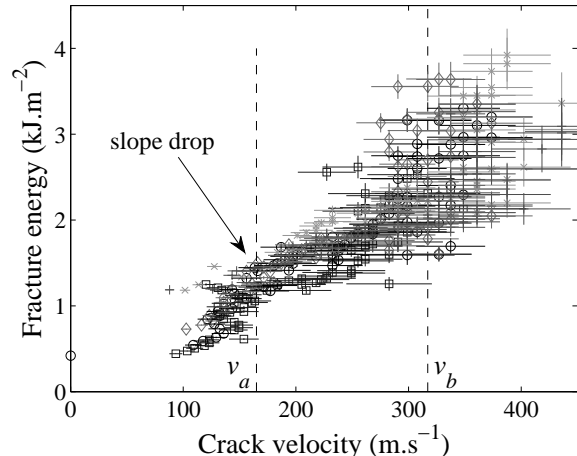


FIG. 1. Fracture energy  $\Gamma$  as a function of macroscale crack velocity  $v$  (adapted from [6]). Different symbols correspond to different experiments. The two vertical dashed lines correspond to  $v_a$  (microcracking onset) and  $v_b$  (microbranching onset). Below  $v_b$ , all the experimental points collapse onto a single  $\Gamma(v)$  curve. The slope of this curve exhibits a drop at  $v_a$ .

Recent experiments using PMMA showed that, above  $v_a$ , the slope of  $\Gamma(v)$  drops [6] (see Fig. 1), suggesting that microcracks make macroscale cracks dissipate less

or/and propagate faster than a single crack would. This is at odds with the common view that damage through opening mode microcracks slows down crack propagation by increasing energy dissipation [3, 7, 14]. Understanding this counterintuitive behaviour requires unravelling the coupling between (i) the space-time dynamics of damage at the FPZ scale and (ii) the crack dynamics at the macroscale. The time interval between two successive microcrack nucleation events is typically a few tens of nanoseconds. This makes real-time local measurements of microcracking dynamics beyond current researchers' reach. Hence, fast crack propagation has been studied only through measurements of the average dynamics of the macroscopic crack front [5–8, 10–16].

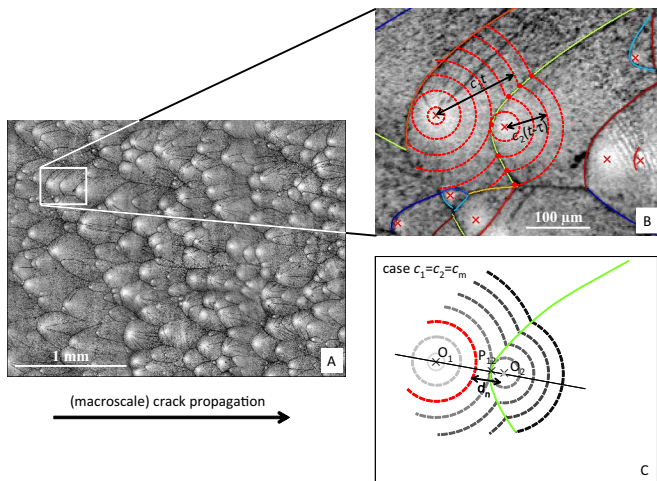


FIG. 2. Fractographic signature of microcracking in the dynamic fracture of PMMA. (A) Typical fractographic microscope image ( $K \simeq 3.10 \pm 0.05 \text{ MPa.m}^{1/2}$ ). Bright regions correspond to microcrack nucleation centers (Materials and Methods). (B) Red dashed circle arcs sketch successive front locations of two interacting microcracks (nucleated at  $t=0$  and  $t=\tau$ ) growing radially at speeds  $c_1$  and  $c_2$ . Fitting of fractographic branches (color lines) with a geometrical model (Eq. (S1)) allows measuring  $c_2/c_1$ . (C) When  $c_2 = c_1$ , markings (green line) are conic branches (Eq. (S2)) and the distance  $d_n$  between the triggered microcrack center and the triggering front at the nucleation time  $t = \tau$  (highlighted in red) is twice the apex-to-focus distance,  $O_2P_{12}$ .

Quantitative fractography is an appealing tool to probe microscale damage mechanisms. Fracture surfaces are indeed known to record fracture processes down to the nanoscale [9, 17]. In particular, in many materials including PMMA (Fig. 2A), microcracks leave characteristic conic-like markings on fracture surfaces [3, 6–9]. These patterns are commonly understood through a geometrical model first developed in [18] and improved in *e.g.* [7, 19]. In this model, each conic-like marking corresponds to the intersection of two penny-shaped microcracks, nucleated at point-like nucleation centers and growing at speeds  $c_1$  and  $c_2$  along two slightly different

planes (Fig. 2B). The numerical implementation of this model demonstrated that microcracking is responsible for some of the complexity of macroscopic crack growth [7], *e.g.* mist fracture surfaces decorated by conic-like markings and strong fluctuations in the velocity signal,  $v(t)$ . However, the agreement remained only qualitative because simplifying prescriptions were used for the microcracking dynamics [7], namely (i) the location of nucleation centers, (ii)  $c_2/c_1$  and (iii) the nucleation criterion.

## EXPERIMENTAL DETERMINATION OF THE DYNAMICS OF INDIVIDUAL MICROCRACKS

Here, we determine experimentally the microscopic rules for the nucleation and growth of microcracks, by analyzing the morphology of each individual conic-like marking on different millimeter-sized fracture surfaces (see *e.g.* Fig. 2A) corresponding to different  $K$  (*i.e.* to different  $v$  in the range  $0.23\text{--}0.49 c_R$ ) (Materials and Methods). We first find that, irrespective of  $K$ , the spatial distribution of nucleation centers is Poissonian (see Fig. 3A, top and Fig. S3), *i.e.* the centers are homogeneously and randomly distributed in space, without correlation. This is consistent with the usual view that microcracks nucleate at some preexisting weak defects randomly distributed within the material's volume, when a crack tip running in their vicinity sufficiently enhances the stress field [3, 9]. The increase in mean surface density of nucleation centers,  $\rho$ , with  $K$  (Fig. 3A, bottom) is attributed to the increase in FPZ size with  $K$ , which yields more volume defects turning into microcracks (see [6] and *SI text*). Because  $\rho$  completely characterizes Poisson distributions, it will be used hereafter as the parameter as a function of which the various quantities will be plotted.

Stationarity of macroscopic crack propagation at the scale of each millimetric-sized image requires the ratio  $c_2/c_1$  of the velocities of two successive microcracks to be 1, on average. A smaller (larger) value would indeed produce a decelerating (accelerating) macroscale crack. This requirement has consequences on the geometry of conic-like markings (see *SI text* and Fig. S2), which were checked: We fitted all individual markings with the shape predicted using the geometrical model (see Fig. 2B and *SI text*), with  $c_2/c_1$  being the only adjustable parameter. Irrespective of  $\rho$ ,  $c_2/c_1$  is found equal to 1 within 4% standard deviation (see Fig. 3B and Fig. S4). In the following, we will neglect the slight dispersion of  $c_2/c_1$  and consider that, for any given  $\rho$ , all microcracks propagate at the same velocity:  $c_2 = c_1 = c_m$ , where  $c_m$  denotes the speed of individual microcracks and *a priori* depends on the macroscopic external loading  $K$  (or equivalently on  $\rho$ ).

In these conditions, the intersection between two microcracks is a true conic. Its focus coincides with the

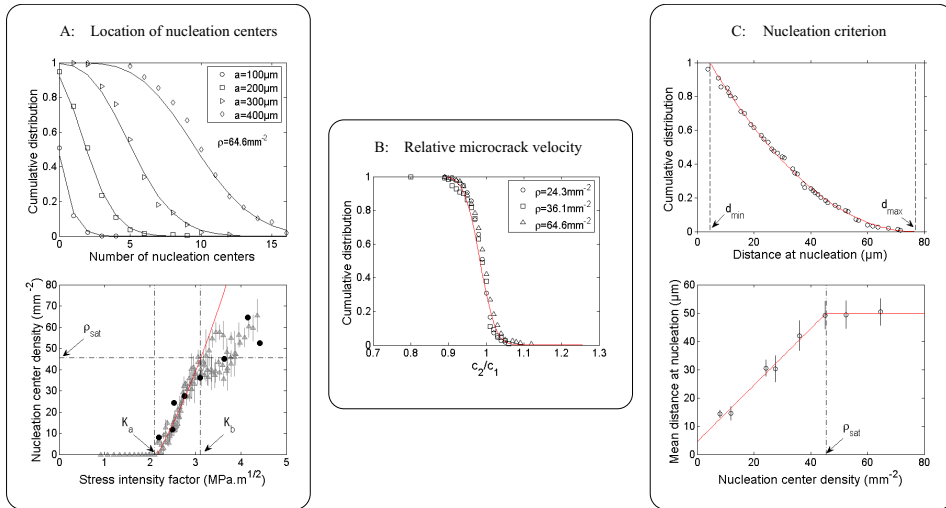


FIG. 3. Microcrack dynamics deduced from fracture surfaces. (A) Top: cumulative distributions for the number of nucleation centers in square regions of size  $a$ , for  $K \simeq 4.15 \pm 0.07 \text{ MPa.m}^{1/2}$ . Solid lines: Poisson function with parameter  $\rho a^2$ . The fitting parameter  $\rho$  is  $a$ -independent, indicating homogeneous uncorrelated random distribution with mean surface density  $\rho$ . Similar results hold for all  $K$  (Fig. S3). Bottom:  $\rho(K)$  curve (black disks) superimposed to that obtained from the data reported in [6] (gray triangles, vertical lines indicate standard deviation). Red line: fit using Eq. (S3) in the range  $K_a = 2.1 \text{ MPa.m}^{1/2} < K < K_b = 3.1 \text{ MPa.m}^{1/2}$  (see *SI text*).  $\rho_{sat} \simeq 45.5 \text{ mm}^{-2}$ . (B) Cumulative distribution, for various  $\rho$ , of the velocity ratio  $c_2/c_1$  obtained via fitting fractographic branches using the geometrical model (see Eq. (S1) and *SI text*). Red line: Fitted normal distribution (average 0.98 and standard deviation 0.03). Similar results hold for each  $\rho$  (Fig. S4). (C) Top: cumulative distribution of  $d_n$  for  $\rho = 27.5 \text{ mm}^{-2}$ . Red line: best two-parameters fit  $P(d_n) = ((d_{max} - d_n)/(d_{max} - d_{min}))^2$ . Here  $d_{min} = 4 \mu\text{m}$ ,  $d_{max} = 77 \mu\text{m}$ . Similar fits hold for all  $\rho$  (Fig. S5). Bottom: mean distance at nucleation  $\bar{d}_n$  as a function of  $\rho$ . Error bars:  $\pm$  one standard deviation. Red line: fit using Eq. (S4) up to a saturating value  $\bar{d}_n \simeq 50 \mu\text{m}$  reached at  $\rho_{sat}$  (see *SI text*).

nucleation center of the triggered microcrack, and the apex-to-focus distance is half the distance  $d_n$  between the triggering front and the triggered center at the instant of nucleation (see Fig. 2C and *SI text*). Hence,  $d_n$  defines the nucleation criterion. Its cumulative distribution is well fitted by a two-parameters parabolic function, irrespective of  $\rho$  (Fig. 3C, top and Fig. S5). Variations of the mean value  $\bar{d}_n$  with  $\rho$  exhibit two regimes: an initial linear increase followed by a saturating plateau, when  $\rho$  exceeds a value  $\rho_{sat}$  (Fig. 3C, bottom). The linear behaviour comes from the fact that  $\bar{d}_n$  and  $\rho$  both scale linearly with the FPZ size (see *SI text*). The transition is understood as the point where  $\bar{d}_n$  becomes comparable with the mean distance between nucleation centers (see *SI text* and Fig. S6).

### DETERMINISTIC RECONSTRUCTION OF THE MICROCRACKING DAMAGE HISTORY

The analyses performed up to now permit a full characterization of the statistics of microcrack nucleation, growth and coalescence within the FPZ. To unravel how this FPZ quantitatively operates to relate the macroscale crack velocity,  $v$ , to the microscale velocity,  $c_m$ , of individual microcracks, we feed the geometrical model with the observed locations of all individual nucleation centers

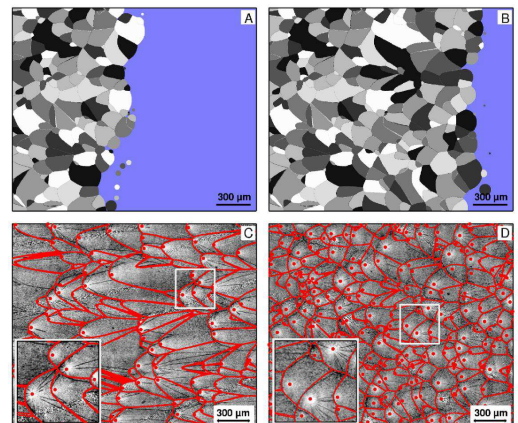


FIG. 4. Deterministic reconstruction of microscale damage and fracture processes. (A-B): successive snapshots of the reconstructed crack propagation and associated conic markings for  $\rho = 64.6 \text{ mm}^{-2}$ . Crack propagates from left to right. (C-D): Fracture surface images (grey level) for (C)  $\rho = 27.5 \text{ mm}^{-2}$  ( $K \simeq 2.77 \text{ MPa.m}^{1/2}$ ) and (D)  $\rho = 64.6 \text{ mm}^{-2}$  ( $K \simeq 4.18 \text{ MPa.m}^{1/2}$ ) compared to the reconstructed conic markings (red lines). Red dots indicate nucleation centers.

and the corresponding distances at nucleation,  $d_n$ . We then simulate the space-time evolution of the fracturing process with the constraint that all microcracks propa-

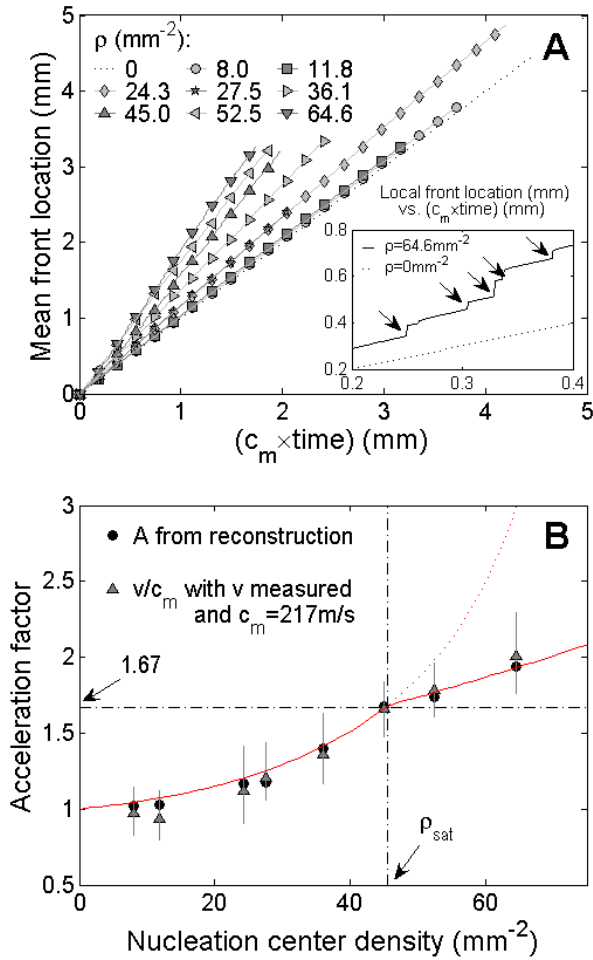


FIG. 5. From slow microcracks to fast collective macroscopic crack motion. (A) Time evolution (scaled by  $c_m$ ) of the average location of the simulated crack front for various  $\rho$ . The fitted slopes of these curves define the acceleration factor  $A$ .  $A=1$  for  $\rho=0$ . Inset: Evolution of the location of a single point of the simulated front, for  $\rho=64.6\text{mm}^{-2}$ , together with that expected for  $\rho=0$  (slope 1). Jumps correspond to coalescence events with microcracks. Between jumps, the slope is close to 1. (B) Black dots: Evolution of the reconstructed acceleration factor  $A$  as a function of  $\rho$ . Triangles: Ratio of the measured macroscopic crack speed,  $v$ , over the microscopic velocity fitted to be  $c_m = 217 \pm 3$  m/s. Error bars indicate the minimum and maximum measured velocities within the considered fractographic image. Thick red line: Eq. 1 with  $b=1.19 \pm 0.02$ . A change in regime occurs for  $\rho = \rho_{sat}$  (vertical dashed line), which corresponds to a velocity of  $1.67 c_m$  (horizontal dashed line).  $\pm$  stands for 95% confidence interval.

gate at the same velocity  $c_1 = c_2 = c_m$  (Materials and Methods). Note that, at this point,  $c_m$  is constant within the FPZ but can depend on  $K$  (or equivalently on  $\rho$ ). Figures 4A-B show typical snapshots of the simulated crack dynamics (see supporting movies). Apart from edge effects (see *SI text* and Fig. S7), the matching between the experimental conics and the simulated ones is quite satisfactory (Fig. 4C-D) for all values of  $\rho$ . As expected, the

simulated dynamics thus provide a deterministic reconstruction of the ultra-fast microcracking dynamics. The spatial resolution of  $\sim 2 \mu\text{m}$  (pixel size) and the time resolution of  $\sim 10$  ns (pixel size divided by  $c_m$ , demonstrated hereafter to be a load-independent constant close to a value  $c_m \sim 200$  m/s) are much beyond standard experimental mechanics methods like acoustic emission or fast imaging. Similar deterministic nucleation and geometrical growth models are used in a broad range of fields including metallurgy [20], biology [21] and superconductivity [22].

## MACROSCALE CRACK DYNAMICS

To shed light on the macroscale effect of microcracking damage, we now focus on the time evolution of the average location of the simulated crack front (Fig. 5A). For each  $\rho$ , this evolution is linear, meaning that the average front has a constant velocity,  $A \times c_m$ , the value of which was found insensitive to edge effects (see *SI text* and Fig. S7). Figure 5B shows that the acceleration factor  $A$  equals 1 only for  $\rho=0$ , and then increases with  $\rho$ . The time evolution of the position of a single point of the front (Fig. 5A) sheds light on the origin of this effective acceleration. The point motion is jerky, with sudden jumps corresponding to microcrack coalescence events, and the velocity between jumps is close to  $c_m$ . Hence, as the rate of coalescence events increases with  $\rho$ ,  $A$  also increases with  $\rho$ . A simple mean-field lattice model, which evaluates the rate of coalescence events, yields (see *SI text* and Fig. S8):

$$A = \frac{1}{1 - b d_n \sqrt{\rho}} \quad (1)$$

where  $b$  is a numerical factor  $\simeq 1$ . This equation, when combined with the observed evolution of  $d_n$  with  $\rho$  (Fig. 3C, bottom, red line), gives the red line in Fig. 5B, which is in very good agreement with reconstructed velocities.

The question remains of the possible dependence of  $c_m$  with  $\rho$ . Figure 5B shows that, if we chose a  $\rho$ -independent  $c_m = 217 \pm 3$  m/s  $= 0.24 \pm 0.01 c_R$ , the  $\rho$ -dependence of the reconstructed acceleration factor  $A$  is identical to the ratio of the measured macroscopic crack speed,  $v$ , over  $c_m$ . This means that the propagation speed of microcracks is not only identical for two successive microcracks, but also all along the crack path, irrespective of  $\rho$  - and hence of  $K$ . Note that  $c_m$  is found very close to the maximum speed,  $\simeq 204$  m/s or  $\simeq 0.23 c_R$ , of individual crack fronts in PMMA originating from the fracture energy increase with FPZ size [6]. The change in the  $\rho$ -dependence of  $A$  observed at  $\rho_{sat}$  in Fig. 5B corresponds to a macroscopic crack speed  $\simeq 1.67 c_m \simeq 0.41 c_R$ . This velocity is very close to the onset of the microbranching instability ( $0.36 c_R$  in PMMA [11]), which suggests that this instability

could be related to the steric effect responsible for the saturation of  $\bar{d}_n(\rho)$  above  $\rho_{sat}$ .

## DISCUSSION

In dynamic fracture, the relationship between the opening force and the speed at which a macroscopic crack moves forward is controlled by dissipative and nonlinear processes that develop at the microscale within the FPZ. The space and time scales associated with the FPZ dynamics are usually too small to enable a real time and space monitoring of these processes. Here, we demonstrate that such a detailed monitoring is actually possible in PMMA, the archetype of nominally brittle materials, by analysing *post mortem* the patterns left on fracture surfaces by microcracking damage.

Our results show that, in PMMA, the true local propagation speed of single cracks is limited to a fairly low value  $c_m$ , about  $0.23c_R$ , while the apparent speed,  $v$ , measured at the continuum-level scale can be much higher. When  $v \geq c_m$ , the macroscopic crack is actually found to progress through the coalescence of microcracks, all growing at the same constant velocity  $c_m$ . The main effect of microcracking damage, therefore, is not, as commonly believed [3, 7, 14], to slow down fracture by increasing the energy required to further propagate a crack, but on the contrary to boost the macroscopic (group) crack velocity to a value larger than what would have been obtained in their absence.

We conjecture that the limiting value  $c_m$  of the local crack speed is set by the material-dependent dissipative and non-linear processes that develop in the highly stressed/strained zones in the very vicinity of the (micro)crack tips, like *e.g.* thermal [23], viscoelastic [15, 24] or hyperelastic [5, 25] processes. As for the subsequent boost from  $c_m$  to the continuum-level scale velocity  $v$ , it is shown here to take the form of a purely geometric factor controlled by two microscopic quantities: (i) The density of nucleation centers  $\rho$  and (ii) the mean distance at nucleation  $\bar{d}_n$ . These two internal variables characterize the damaging state, and evolve with the amount of mechanical energy flowing into the FPZ. As such, they are material-dependent functions of the external loading  $K$ , the knowledge of which permits to fully relate  $v$  and  $c_m$ .

This enhanced description of dynamic brittle fracture, demonstrated on PMMA, can likely be extended qualitatively to all materials involving propagation-triggered microcracks, *e.g.* oxide glass [3, 26], polymeric glasses [3, 9], polycrystals [3], rocks [27, 28] and bones [29]. Further work is required to check this conjecture, and subsequently to quantitatively determine how  $c_m$ ,  $\rho$  and  $\bar{d}_n$  are selected in these materials. From the geometric nature of the acceleration factor, we also anticipate that fast macroscopic cracks in other fracture modes could simi-

larly originate from the collective motion of many slow microcracks.

## MATERIALS AND METHODS

### Experiments

Fracture surfaces were obtained from the experiments described in reference [6]. Dynamic cracks were driven in PMMA (Young's modulus  $E = 2.8$  GPa and Poisson's ratio  $\nu = 0.36$ , yielding a Rayleigh wave speed  $c_R = 880$  m/s) using the Wedge-Splitting geometry sketched in Fig. S1. Specimens were prepared from parallelepipeds of size  $140 \times 125 \times 15$  mm<sup>3</sup> in the propagation, loading, and thickness directions, respectively. Subsequently, a notch was formed (i) by cutting a  $25 \times 25$  mm<sup>2</sup> rectangle from the middle of one of the  $125 \times 15$  mm<sup>2</sup> edges; and (ii) by subsequently adding a 10 mm groove deeper into the specimen. A circular hole with a radius ranging between 2 and 8 mm was eventually drilled at the tip of the groove. Two steel jaws equipped with rollers were placed on both sides of the rectangular cut-out and a steel wedge of semi-angle 15 degrees was pushed between them at constant velocity 38 m/s up to crack initiation. Crack speed was measured using a modified version of the potential drop technique: A series of 90 parallel conductive lines (2.4 nm-thick Cr layer covered with 23 nm-thick Au layer), 0.5 mm wide with a period of 1 mm (space accuracy 40  $\mu$ m) were deposited on one of the two  $140 \times 125$  mm<sup>2</sup> sides of the specimen, connected in parallel and alimented with a voltage source. As the crack propagated, the lines were cut at successive times detected with an oscilloscope (time accuracy 0.1  $\mu$ s) and allowed to record the instantaneous macroscopic crack velocity  $v$ , with better than 10% accuracy. The variations of the quasi-static stress intensity factor  $K$  were computed using 2D finite element calculations (software CASTEM 2007) on the exact experimental geometry, assuming plane stress conditions, and a constant wedge position throughout failure of the specimen. Values for the fracture energy  $\Gamma$  were directly obtained from the equation of motion  $\Gamma \approx (1 - v/c_R)K^2/E$  by combining the  $v$  measurements and the  $K$  calculations.

*Post mortem* topography images were obtained with an optical profilometer (M3D, Fogale Nanotech,  $\times 5$  objective yielding square pixels of size 1.86  $\mu$ m) at various locations along the fracture surfaces in different broken specimens - each zone of observation is characterized by a given value of  $K$ . For each location, nine neighbouring images were gathered to provide an observation field of at least  $2 \times 2$  mm<sup>2</sup>, large enough to carry out statistical analyses. The presence of a highly reflective area at the focus of each conic-like marking results from plastic deformations at microcrack nucleation and allows locating unambiguously all nucleation centers (see Fig. 2A). For

many microcracks, fragmentation lines focusing on the nucleation center were also observed, and helped increasing the accuracy of the location. For each marking, we made an initial guess about which microcrack triggered its nucleation. The apex of the marking was defined as the intersection between the segment linking the triggering and triggered centers and the conic-like marking. A new guess was made if the simulated marking did not resemble the observed one.

### Simulation

The macroscopic crack front was initially straight, vertical and located on the left of the image. It started propagating towards the right at constant velocity (1 pixel/time step). When the macroscopic crack front reached a distance  $d_n$  from the closest nucleation center, a microcrack was nucleated and made grow radially at the same velocity. The total front was then made of both the initially straight translating front and the newly created radially growing circular front. When these two coincided, propagation was continued in the unbroken part of the specimen only. Intersection points defined the conic-like marking. The same procedure was applied each time the shortest distance between the total front and another nucleation center was found to have decreased down to the distance at nucleation  $d_n$  associated with this center. Edge effects were minimized in the evaluation of  $A$  by considering only the times after all points of the initial front coalesced with a nucleated microcrack, and before the first point of the total front reached the right edge of the image.

We thank A. Prevost for his help with the profilometry measurements. We thank K. Ravi-Chandar for helpful discussions. We thank L. Barbier, G. Debrégeas, A. Malthe-Sorensen, J. Mathiesen, K.J. Måløy, P. Meakin, and C. Rountree for careful reading of the manuscript. We acknowledge funding from French ANR through Grant No. ANR-05-JCJC-0088, from Triangle de la Physique through Grant No. 2007-46, from Mexican CONACYT through Grant No. 190091 and from the European Union through Marie Curie grant No. PIEF-GA-2009-237089. This Letter was supported by a Center of Excellence grant to PGP from the Norwegian Research Council.

- 
- [1] Freund LB (1990) *Dynamic Fracture Mechanics* (Cambridge University Press, Cambridge, England).  
 [2] Fineberg J, Marder M (1999) Instability in dynamic fracture. *Phys. Rep.* 313:1-108.  
 [3] Ravi-Chandar K (2004) *Dynamic Fracture* (Elsevier, Amsterdam, The Netherlands).

- [4] Cox B, Gao HJ, Gross D, Rittel D (2005) Modern topics and challenges in dynamic fracture. *J. Mech. Phys. Solids* 53:565-596.  
 [5] Livne A, Bouchbinder E, Svetlizky I, Fineberg J (2010) The near-tip fields of fast cracks. *Science* 327:1359-1363.  
 [6] Scheibert J, Guerra C, Célerié F, Dalmas D, Bonamy D (2010) Brittle-quasibrittle transition in dynamic fracture: An energetic signature. *Phys. Rev. Lett.* 104:045501.  
 [7] Ravi-Chandar K, Yang B (1997) On the role of microcracks in the dynamic fracture of brittle materials. *J. Mech. Phys. Solids* 45:535-563.  
 [8] Ravi-Chandar K (1998) Dynamic fracture of nominally brittle materials. *Int. J. Fracture* 90:83-102.  
 [9] Hull D (1999) *Fractography: Observing, measuring and interpreting fracture surface topography* (Cambridge University Press, Cambridge, England).  
 [10] Sharon E, Gross SP, Fineberg J (1995) Local crack branching as a mechanism for instability in dynamic fracture. *Phys. Rev. Lett.* 74:5096-5099.  
 [11] Sharon E, Fineberg J (1999) Confirming the continuum theory of dynamic brittle fracture for fast cracks. *Nature* 397:333-335.  
 [12] Bergkvist H (1974) Some experiments on crack motion and arrest in polymethylmethacrylate. *Eng. Fract. Mech.* 6:621-622.  
 [13] Goldman T, Livne A, Fineberg J (2010) Acquisition of inertia by a moving crack. *Phys. Rev. Lett.* 104:114301.  
 [14] Washabaugh PD, Knauss W (1994) A Reconciliation of dynamic crack velocity and Rayleigh-wave speed in isotropic brittle solids. *Int. J. Fracture* 65:97-114.  
 [15] Boudet JF, Ciliberto S, Steinberg V (1996) Dynamics of crack propagation in brittle materials. *J. Phys. II* 6:1493-1516.  
 [16] Rosakis AJ, Samudrala O, Coker D (1999) Cracks faster than the shear wave speed. *Science* 284:1337-1340.  
 [17] Kermodé JR, et al. (2008) Low-speed fracture instabilities in a brittle crystal. *Nature* 455:1224-1227.  
 [18] Smekal A (1953) Zum Bruchvorgang bei sprödem Stoffverhalten unter ein- und mehrachsigen Beanspruchungen. *Oesterr. Ing. Arch.* 7:49.  
 [19] Rabinovitch A, Belizovsky G, Bahat D (2000) Origin of mist and hackle patterns in brittle fracture. *Phys. Rev. B* 61:14968.  
 [20] Mukhopadhyay P, Loeck M, Gottstein G (2007) A cellular operator model for the simulation of static recrystallization. *Acta Mater.* 55:551-564.  
 [21] Jettstuen E, Nermoen A, Hestmark G, Timdal E, Mathiesen J (2010) Competition on the rocks: Community growth and tessellation. *PLoS ONE* 5:e12820.  
 [22] Vestgarden JI, Shantsev DV, Galperin YM, Johansen TH (2008) Flux distribution in superconducting films with holes. *Phys. Rev B* 77:014521.  
 [23] Estevez R, Tijssens MGA, Van der Giessen E (2000) Modeling of the competition between shear yielding and crazing in glassy polymers. *J. Mech. Phys. Solids* 48:2585-2617.  
 [24] Persson BNJ, Brener EA (2005) Crack propagation in viscoelastic solids. *Phys. Rev. E* 71:036123.  
 [25] Buehler MJ, Abraham FF, Gao, HJ (2003) Hyperelasticity governs dynamic fracture at a critical length scale. *Nature* 426:141-146.  
 [26] Rountree CL, et al. (2002) Atomistic aspects of crack propagation in brittle materials: Multimillion atom molecular dynamics simulations. *Ann. Rev. Mater. Res.*

- 32:377-400.
- [27] Moore DE, Lockner DA (1995) The role of microcracking in shear-fracture propagation in granite. *J. Struct. Geol.* 17:95-114.
- [28] Kobchenko M, Panahi H, Renard F, Dysthe DK, Malthé-Sorensen A, Mazzini A, Scheibert J, Jamtveit B, Meakin P (2011) 4D imaging of fracturing in organic-rich shales during heating. *J. Geophys. Res.* doi:10.1029/2011JB008565, in press.
- [29] Nalla RK, Kinney JH, Ritchie RO (2003) Mechanistic fracture criteria for the failure of human cortical bone. *Nat. Mater.* 2:164-168.